Met. Mater. Int., Vol. 18, No. 2 (2012), pp. 201~207
doi: 10.1007/s12540-012-2001-y Published 27 April 2012

Kinetics of Cr/Mo-rich Precipitates Formation for 25Cr-6.9Ni-3.8Mo-0.3N Super Duplex Stainless Steel

Sang-Ho Byun[1], Namhyun Kang[1,*], Tae-Ho Lee[2], Sang-Kon Ahn[3], Hae Woo Lee[4], Woong-Seong Chang[5], and Kyung-Mox Cho[1]

[1]Department of Materials Science and Engineering, Pusan National University, Busan 609-735, Korea
[2]Korea Institute of Materials Science, Changwon 641-010, Korea
[3]Stainless Steel Research Group, POSCO Technical Research Laboratories, Pohang 790-785, Korea
[4]Department of Materials Science and Engineering, Dong-A University, Busan 604-714, Korea
[5]Research Institute of Industrial Science and Technology, Pohang 790-600, Korea

(received date: 15 April 2011 / accepted date: 15 July 2011)

The amount and composition of Cr-rich (σ) and Mo-rich (χ) precipitates in super duplex stainless steels was analyzed. An isothermal heat treatment was conducted at temperatures ranging from 700 °C to 1000 °C for up to 10 days. A time-temperature transformation (TTT) diagram was constructed for the mixture of σ and χ phases. The mixture of the σ and χ phases exhibited the fastest rate of formation at approximately 900 °C. Minor phases, such as Cr_2N, $M_{23}C_6$, and M_7C3, were also detected using a transmission electron microscopy (TEM). Also, a continuous cooling transformation (CCT) diagram was constructed for the mixture of σ and χ phases using the Johnson-Mehl-Avrami equation. Compared with the known CCT diagram of the σ phase, this study revealed faster kinetics with an order of magnitude difference and a new CCT diagram was also developed for a mixture of σ and χ phases. The calculated fraction of σ and χ phases obtained at a cooling speed of 0.5 °C/s was in good agreement with the experimental data.

Key words: metals, annealing, microstructure, transmission electron microscopy (TEM), precipitation

1. INTRODUCTION

Due to the recent increases in energy consumption, the facilities that generate electric power via nuclear and thermal energy need to be expanded. Furthermore, petroleum chemical facilities are exposed to severe operational environments, such as high temperatures and seawater corrosion, which induce pitting, crevice corrosion, and stress corrosion cracking. In order to overcome the harsh environment, super duplex stainless steels (SDSSs) have been developed through the reformation of alloy elements from conventional duplex stainless steels (DSSs). The SDSSs originally consist of austenite and ferrite; however, Cr- and Mo-rich intermetallic compounds (IMCs) are formed when the SDSSs are exposed to high temperature environments [1-5]. Ramirez *et al.* and Qiu and Zhang. reported the precise kinetics of Cr_2N and secondary austenite [6-8]. The enrichment of Cr and Mo in the intermetallic precipitates reduced the corrosion resistance and toughness [9,10] because the formation of the σ phase and χ phase produced a region of Cr and Mo depletion near the precipitate during the exposure to high temperatures. In particular, the welding on the SDSSs affected the heat affected zone and created the σ phase and χ phase [11-13]. Although the continuous cooling transformation (CCT) diagram of the σ phase was produced previously using optical microscopy [8,14], the color etching method in the optical microscopy produced some scattering error. Moreover, the CCT diagram was either not confirmed experimentally for the detrimental χ phase [8] or was only estimated by the optical microstructure [14].

The study constructed time-temperature transformation (TTT) and CCT diagrams to examine the kinetics of the (σ+χ) formation in SDSSs. The phase was identified using a wavelength dispersive spectroscopy (WDS) and transmission electron microscopy (TEM) with a selected area diffraction (SAD). The backscattered electron (BSE) image in the electron probe microanalysis (EPMA) provided more precise phase quantification than the color etching determined using the optical microscopy. Specifically, the constructed CCT diagram of the (σ+χ) formation was confirmed through continuous cooling experiments as a function of the cooling speed.

*Corresponding author: nhkang@pusan.ac.kr

2. EXPERIMENTAL PROCEDURES

Super duplex stainless steels (SDSSs) with a composition of 25Cr-6.9Ni-3.8Mo-0.3N were used. The isothermal heat treatment was executed at 700 °C, 730 °C, 750 °C, 800 °C, 850 °C, 900 °C, 950 °C, and 1000 °C. The heat treatment was conducted for different time periods (10 minutes, 30 minutes, 60 minutes, 3 days, 7 days, and 10 days) followed by water quenching. The 10, 30, and 60 minute heat treatments were performed in a salt bath, whereas the heat treatments for periods more than 3 days were performed in a box furnace purged with Ar gas. In order to verify the calculated phase kinetics in the CCT, the real microstructure was observed from the continuous cooling experiment after heating to 1100 °C, followed by a determined cooling speed, such as 10 °C/s, 1 °C/s, 0.5 °C/s, and 0.1 °C/s.

The specimen was polished with 1 μm diamond paste and electrolytic etched in a 10 wt% oxalic acid solution (2.7 V for 10 seconds). The σ phase and χ phase were identified via WDS and confirmed using SAD. The quantitative analysis of the phase fraction was performed using the BSE image in the EPMA. Five randomly dispersed BSE images were used for the quantitative measurement of the phase fraction. The thin foils for the TEM examination were prepared via a twin-jet method with a 15% perchloric acid and 85% methanol electrolyte at –20 °C. The thin foils were then examined via scanning TEM (STEM; JEM 2100F, JEOL, Japan) at 200 kV. Detailed analyses of the SAD patterns were undertaken using Desktop Microscopist V2.2 software (Lucuna Lab., USA).

A time-temperature transformation diagram for a mixture of σ and χ phases was produced from the isothermal heat treatment. The isothermal heat treatment period was converted to a continuous period using the Avrami equation [15], as described in Eq. (1). This equation sets the formation starting and completion points to 0 and 1, respectively.

$$f = V/V_e = 1 - \exp(-kt^n), \tag{1}$$

where f denotes the calculated transformation fraction, k is the reaction constant, and the exponent n is a constant determined by the transformation mechanism of the nuclear formation and growth. In order to calculate the fraction (f) after transformation, the equilibrium fraction (V_e) must be measured as the saturated fraction with respect to time. The equilibrium fraction (V_e) was measured using the isothermal heat treatment over an extremely long time, i.e. 10 days in this study. The constants n and k were calculated using Eqs. (2) and (3). t_1 and t_2 indicate the isothermal maintenance time for each step, respectively. In addition, the fraction at that time is shown with V_1 and V_2, respectively.

$$n = \frac{\left(\frac{\ln(1-V_1/V_e)}{\ln(1-V_2/V_e)}\right)}{\ln t_1/t_2}. \tag{2}$$

$$k = \frac{-\ln(1-V_1/V_e)}{t_1^n}. \tag{3}$$

A CCT diagram for the formation of the σ and χ phases was produced using the modified Avrami (Johnson-Mehl-Avrami) equation in Eq. (4). Detailed procedures were followed from previous studies [13, 14]. τ_i is the time consumed in step i to begin the formation and the time to create a V_{i-1} fraction. The τ value was calculated using Eq. (5). The n_i and k_i values are the same as those for the TTT calculation. V_{ei} is the equilibrium fraction at a temperature of i.

$$f_i = V_i/V_{ei} = 1 - \exp[-k_i(\tau_i + \Delta t)^{n_i}]. \tag{4}$$

$$n = \frac{\left(\frac{\ln(1-V_1/V_e)}{\ln(1-V_2/V_e)}\right)}{\ln t_1/t_2}. \tag{5}$$

3. RESULTS AND DISCUSSION

3.1. Microstructural behavior of annealing at 850 °C

Figure 1(a) shows the optical microstructure prior to heat treatment. The as-rolled microstructure consisted of 50%

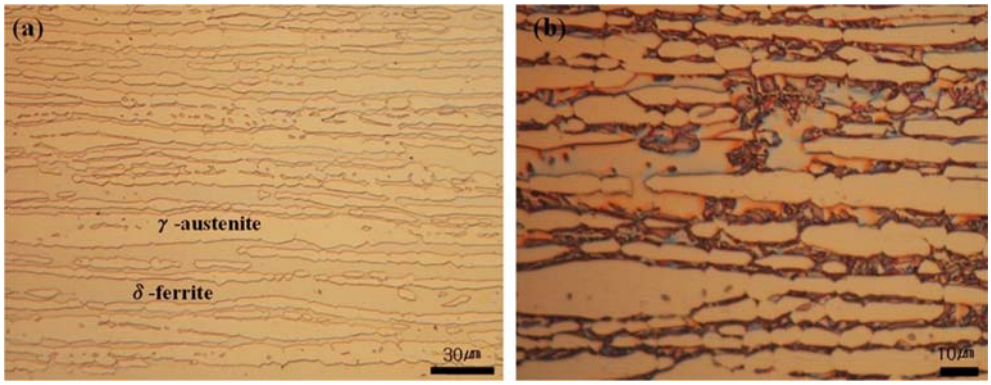

Fig. 1. Microstructure of the SDSS; (a) as-rolled and (b) annealed at 850 °C for 10 minutes.

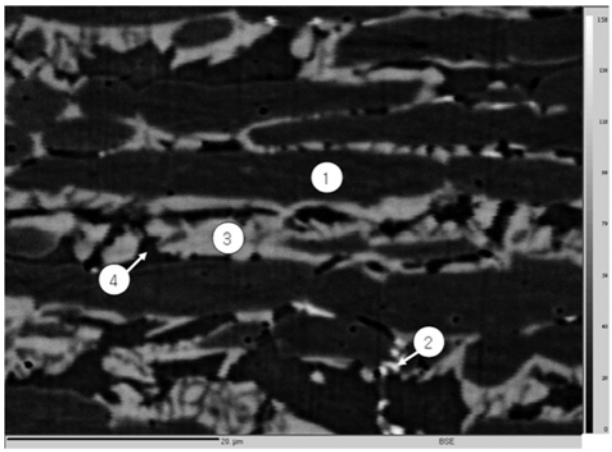

Fig. 2. The EPMA-BSE microstructure annealed at 850 °C for 10 minutes.

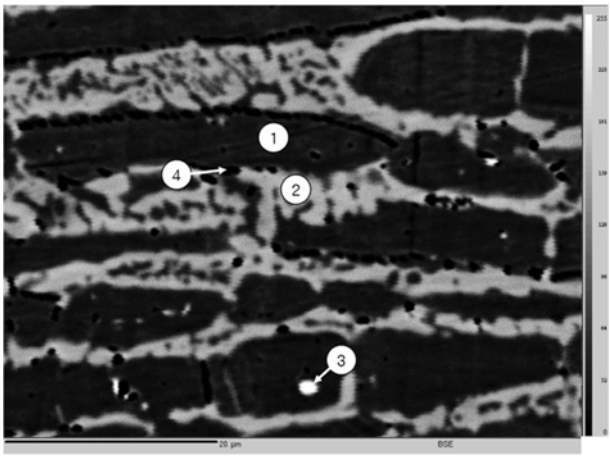

Fig. 3. The EPMA-BSE microstructure annealed at 850 °C for 3 days.

austenite and 50% ferrite, whose grains were elongated parallel to the rolling direction. Figure 1(b) illustrates the microstructure after the isothermal heat treatment at 850 °C for 10 minutes. A new phase with a dark brown color appeared in the ferrite matrix and is believed to be a sigma (σ) or chi (χ) phase. However, it is difficult to quantitatively determine the amount of σ and χ phases using optical microscopies. This is because the phase fraction in the etched samples measured via the optical microscopy could be affected by the degree of etching and annealing conditions.

Figure 2 shows the BSE microstructure for the same specimen annealed isothermally at 850 °C for 10 minutes. The WDS analysis revealed the dark gray and black areas to be austenite and ferrite, respectively, as shown in Table 1. The secondary phases embedded in the ferrite had a high Cr and Mo content, and produced bright shades, such as light grey (σ) and white (χ), respectively. The σ phase with a high Cr content was the primary component, and the χ phase with a high Mo content and the largest atomic weight was found in small amounts. Cr and Mo substituted for Fe in the ferrite matrix and had a large atomic radius and restricted diffusivity, even at high temperatures (850 °C). Therefore, the σ and χ phases were located primarily at the boundary between austenite and ferrite. This phenomenon was more dominant for the χ phase than the σ phase.

Figure 3 shows the amount of secondary phases as a function of the annealing time (3 days); Table 2 lists the composition of each phase depicted in Fig. 3. Austenite, ferrite, σ phases, and χ phases were detected. The ferrite components were replaced by Cr_2N in the black area, secondary austenite (γ_2) in dark grey area, and a mixture of (σ+χ) phases in the grey area. Moreover, the χ phase of the white area was found in the austenite matrix. Based on the calculated equilibrium phase diagram using Thermo-Calc. software, the phase fraction of ferrite and austenite was approximately 50:50 at 1150 °C (Fig. 4). Below 1150 °C, the phase fraction of ferrite decreased and that of austenite increased. The σ phase began to form below 1000 °C. Therefore, the annealing process at 850 °C increased the concentration of austenite, σ phase, and Cr_2N. The ferrite was consumed through an eutectoid reaction ($\delta \rightarrow \gamma_2+\sigma$). The eutectoid reaction occurred preferentially at the ferrite and austenite interface due to the rapid diffusion. Therefore, the γ_2 and σ phases primarily remained along the interface. As the annealing time increased from 10

Table 1. Composition of the microstructure annealed at 850 °C for 10 minutes (WDS)

	Si	Cr	Mn	Ni	C	Mo	N	Phase identification
1	0.3	27. 6	0.6	8.2	0.0	2.8	1.1	Dark gray (austenite)
2	0.4	28.7	0.6	4.2	1.4	11.5	0.8	White (χ)
3	0.4	32.8	0.4	3.8	0.8	6.8	0.4	Light gray (σ)
4	0.3	29.5	0.4	3.3	0.0	2.2	0.4	Black (ferrite)

Table 2. Composition of microstructure annealed at 850 °C for 3 days (WDS)

	Si	Cr	Mn	Ni	C	Mo	N	Phase identification
1	0.3	26.9	0.6	7.8	0.0	2.8	1.1	Dark grey (austenite)
2	0.4	33.2	0.5	4.1	1.3	6.7	0.4	Grey (σ)
3	0.4	31.6	0.5	4.1	0.0	10.9	0.5	White (χ)
4	0.3	40.9	0.3	3.8	1.3	5.4	6.0	Black (Cr_2N)

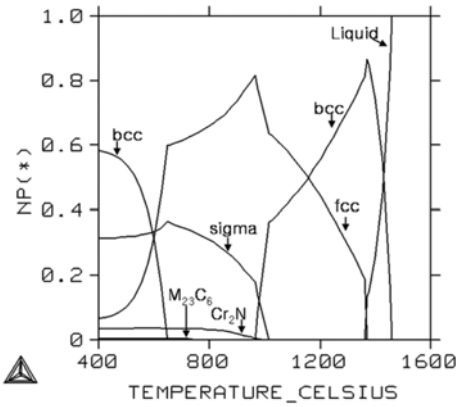

Fig. 4. Phase fractions for the SDSS.

minutes to 3 days, the s and c phases were also precipitated in the austenite matrix due to the significant diffusion of Cr and Mo.

3.2. TEM analysis of the intermetallic precipitates

The intermetallic precipitates produced by the isothermal heat treatment of the SDSSs were identified via TEM. Figure 5 shows the bright field (BF) images that exhibit the precipitation of the second phases and corresponding SAD patterns. The isothermal heat treatment at 800 °C for 10 minutes resulted in the precipitation of second phases with a coarse and irregular morphology along the grain boundaries. The SAD revealed the second phases to be intermetallic χ and σ phases. In many transition metal systems, the χ phase is normally associated with the σ phase, and it belongs to topologically close-packed (TCP) phases. The χ phase is frequently identified as a ternary compound containing Fe, Cr, and Mo, corresponding to $Fe_{36}Cr_{12}Mo_{10}$. The crystal structure of the χ phase was reported to have a *bcc* α-Mn type crystal structure, and the lattice parameter in the Fe-Cr-Mo system has been determined as $a = 0.892$ nm [16].

Another intermetallic phase that formed along the austenite/ferrite boundaries was identified as the σ phase. The morphology of the σ phase was a coarse and irregular block shape with a darker contrast than the χ phase. The mean size and volume fraction of the σ phase increased with heat treatment time. The crystal structure of the σ phase was confirmed to be a tetragonal unit cell ($c/a = 0.52$; 30 atoms per unit cell) of space group $P4_2/mnm$ with $a = 0.880$ and $c = 0.454$ nm [16]. Analyses of the SAD patterns from various zone axes exhibited no distinct orientation-based relationship with ferrite or austenite. In some cases, small precipitates (< 1 μm) were also identified along the austenite/ferrite boundaries, even though the EPMA-BSE analysis failed to locate them. The SAD identified the second phase to be $M_{23}C_6$ carbide (Fig. 5(c)), whose crystal structure is a complex cubic (*fcc*) structure with a lattice parameter of 1.060 nm. $M_{23}C_6$ is related to the lattice of an adjacent austenite grain in accordance with the cube-cube orientation relationship.

Figure 6 shows the TEM images of the specimen annealed isothermally at 800 °C for 7 days. Regardless of the annealing time, the σ and χ phases were consistently observed along the austenite/ferrite boundaries and their size increased with the annealing time. Two important features were observed after prolonged annealing: small particles precipitated within

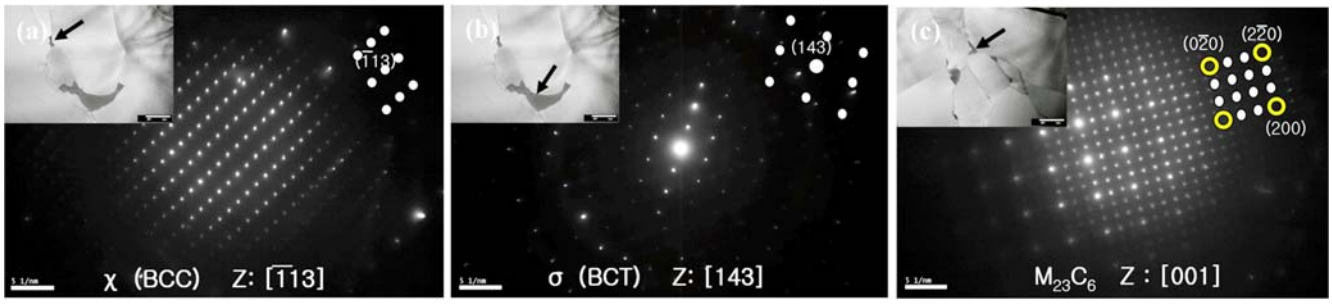

Fig. 5. TEM micrographs of the second phases formed at 800 °C for 10 minutes: (a) χ phase, (b) σ phase, and (c) $M_{23}C_6$ carbide.

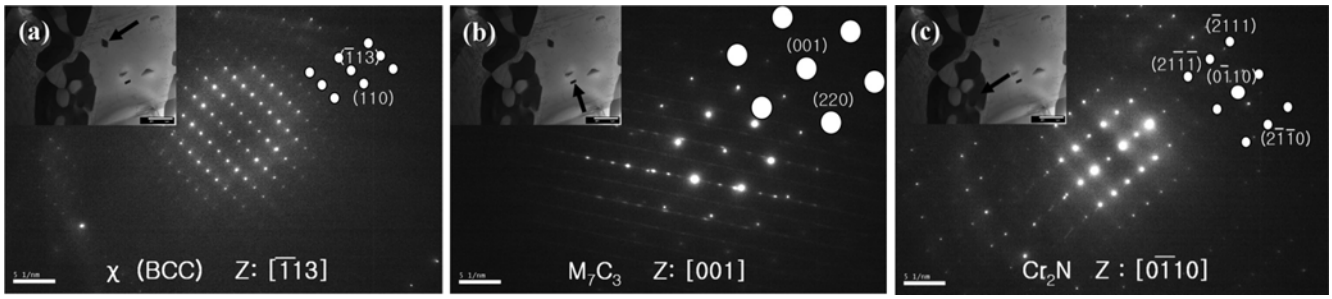

Fig. 6. TEM micrographs at 800 °C after 7 days showing the (a) χ phase, (b) M_7C_3, and (c) Cr_2N.

the grain interior and a coarse nitride formed primarily at the grain boundaries in addition to the pre-existing σ and χ phases. Figures 6(a) and 6(b) show the BF images of the intragranular precipitates along with the corresponding SAD patterns. The rectangular precipitate shown in Fig. 6(a) was identified as an intermetallic χ phase, suggesting that it forms both at the grain interior and grain boundaries. Another intragranular precipitate with a fine platelet morphology was identified as M_7C_3 carbide, whose crystal structure was orthorhombic and belonging to space group *Pnma* (a = 0.4526, b = 0.7010, and c = 1.2142 nm) [16]. The characteristic streaks were clearly observed in the SAD pattern in Fig. 6(b) due to the existence of the planar defects along the $\{1\bar{1}00\}$ direction. This is because a long annealing time (approx. 7 days) can provide sufficient time to diffuse the substitutional (Cr, Mo) and interstitial (C, N) atoms into the inside of the grain. The coarse and irregular precipitate was also observed along the grain boundaries, as shown in Fig. 6(c). The crystal structure of Cr_2N with a trigonal structure was confirmed based on the SAD pattern (space group: $P\bar{3}1m$; a = 0.4796 and c = 0.4470 nm) [16].

Overall, the EPMA (Figs. 2 and 3) and TEM (Figs. 5 and 6) data confirmed the coincidence of the types and locations of the intermetallic compounds (σ and χ phases), which were the dominant precipitates over carbides. Therefore, the EPMA analysis is a reliable method for quantifying intermetallic compounds.

3.3. TTT and CCT diagrams of intermetallic precipitates (σ and χ phases)

The fraction of σ and χ phases was measured using the EPMA-BSE as a function of the annealing temperature and time. Although the EPMA-BSE could quantify the intermetallic phases, it remained difficult to differentiate between the secondary austenite and sigma phase created within the ferrite matrix and between a small amount of χ phase and abundant σ phase. Therefore, the sum of the σ and χ phases on the BSE images was measured using image analysis software. The images were taken at 1000x magnification in five random places. Table 3 lists the amount of σ and χ phase mixtures.

The isothermal heat treatment from 10 minutes to 3 days showed a linear increase in the quantity of intermetallic precipitates (σ+χ). However, the amount of intermetallic phases barely increased as the annealing time increased to more than 7 days. The sum of the abundant σ phases and small amount of χ phase was adapted to Eq. 1 to fit the continuous annealing time. Figure 7 shows the fraction of intermetallic phases transformed during the isothermal heat treatment. The initiation and end points of the phase transformation were set to 0 and 1, respectively.

Figure 8 shows the time-temperature transformation (TTT) diagram created by converting the Avrami curves (Fig. 7). The TTT diagram shows the 1%, 50%, and 99% curve of the

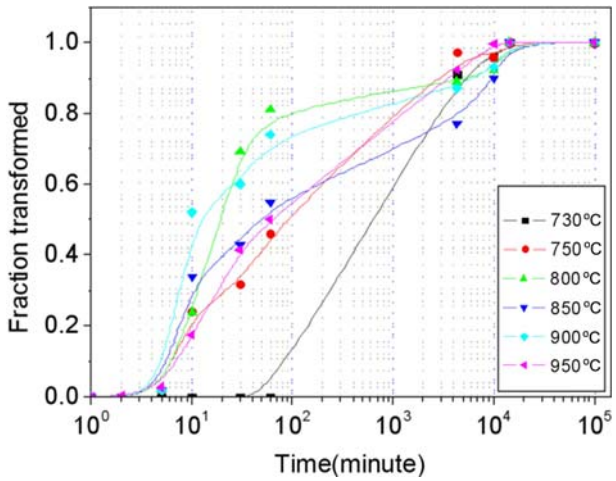

Fig. 7. Avrami curves calculated for phase transformed.

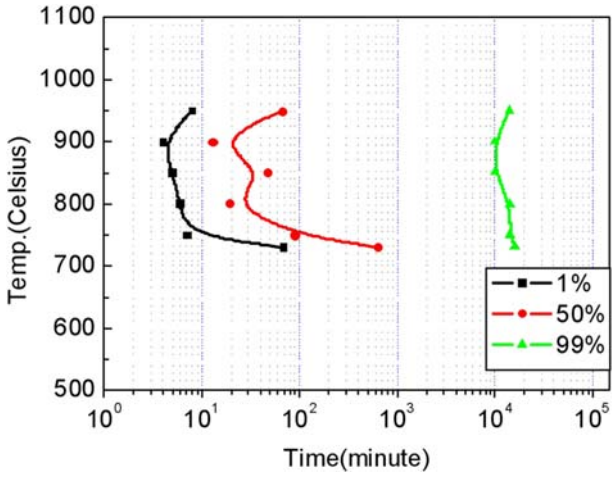

Fig. 8. Experimental TTT diagram of the SDSS.

Table 3. Volume fraction of sigma and chi phases in the SDSS with respect to annealing time and temperature

Time (min)	730 °C	750 °C	800 °C	850 °C	900 °C	950 °C
10	0	10.0±1	12.6±1	16.0±5	25.3±2	6.24±2
30	0	13.4±2	35.9±5	20.3±2	29.3±2	14.7±2
60	0	19.2±5	41.7±6	25.7±5	35.9±6	17.8±4
4320	34.6±5	40.6±6	45.8±3	35.9±4	42.2±5	32.9±5
10080	36.7±6	40.2±4	47.5±2	41.9±4	45.4±4	35.5±2
14400	38.0±5	41.8±2	51.7±2	46.8±3	48.5±4	35.7±2

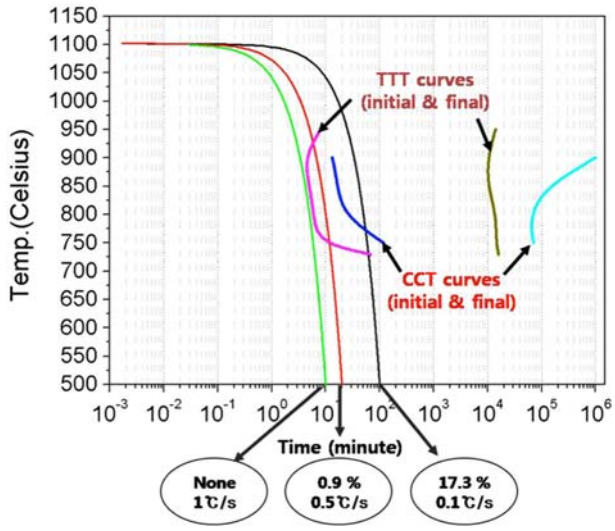

Fig. 9. CCT curves in the range of cooling rates (1 °C/s to 0.1 °C/s).

(σ+χ) phases formed. The nose section, where the fastest transformation occurred, was observed at approximately 900 °C. This study produced a nose section of the σ phase in a short annealing time (5 minutes), which contrasts with the 60 minutes reported previously by Kim *et al.* [14]. The composition of the two studies was similar. The difference in the nose appearance was a result of this study including the (σ+χ) phase fractions. The TTT diagram developed by Nilsson *et al*. [8] was also similar to this study. The previous study included only the σ phase in the TTT diagram, which explains the nose appearance at a longer annealing time than that of this study. However, the SAF2507 sample in this study had a lower Cr content than that in the previous study [8]. Overall, the current study produced a reliable TTT diagram of the (σ+χ) phases.

A CCT diagram for the formation of the (σ+χ) phases was produced using the modified Avrami (Johnson-Mehl-Avrami) equation (4), as indicated in Fig. 9. The initial (1% transformation) and final (99% transformation) CCT curves were moved to the right and down compared with those of the TTT curves. In particular, the continuous cooling curves for 1 °C/s, 0.5 °C/s, and 0.1 °C/s were included in the CCT diagram. A continuous cooling heat treatment was conducted to confirm the validity of the CCT diagram, and the microstructure is shown in Fig. 10. The fraction of (σ+χ) phases was measured as a function of the cooling speeds (1 °C/s, 0.5 °C/s, and 0.1 °C/s). No secondary phases, such as σ and χ phases, were observed at a cooling speed of 1 °C/s, as shown in Fig. 10(a). The σ and χ phases were observed as a light gray color on the BSE images when the cooling speed was decreased to 0.5 °C/s. The amount of (σ+χ) phases was 0.9 %. At the lowest cooling speed of 0.1 °C/s, the phase fraction of (σ+χ) increased to 17.3 %. The initial CCT diagram was in good agreement with the experimental observation examined at 0.5 °C/s. Overall, this study produced a reliable CCT diagram of the (σ+χ) phases. This CCT diagram can be used to predict the formation of secondary phases for welding and heat affected zones.

4. CONCLUSIONS

An isothermal heat treatment of SDSS was performed, and TTT and CCT diagrams of the (σ+χ) phases were produced. The sigma (σ) and chi (χ) phases were created primarily from the austenite and ferrite interface, respectively, and they also appeared within the ferrite matrix. The secondary phases were precisely quantified using the EPMA (BSE, WDS) and TEM (SADP). A longer annealing time increased the amount of the secondary phases (σ+χ). As the annealing time continued for more than 7 days, the formation of the σ and χ phases was almost complete. For annealing at 800 °C, a short annealing time (10 minutes) produced $M_{23}C_6$, whereas long annealing time (> 7 days) produced M_7C_3 and Cr_2N.

A reliable TTT diagram of the (σ+χ) phases was produced using the Avrami equation. A nose of (σ+χ) phases was located approximately at 900 °C and one percent of the (σ+χ) phases were formed within a short time, i.e. 5 minutes. The CCT diagram of the continuous cooling was produced using the modified Avrami (Johnson-Mehl-Avrami) equation. At a cooling speed of 0.5 °C/s, the σ and χ phases of 0.9% were examined on the BSE images. The initial curve from the

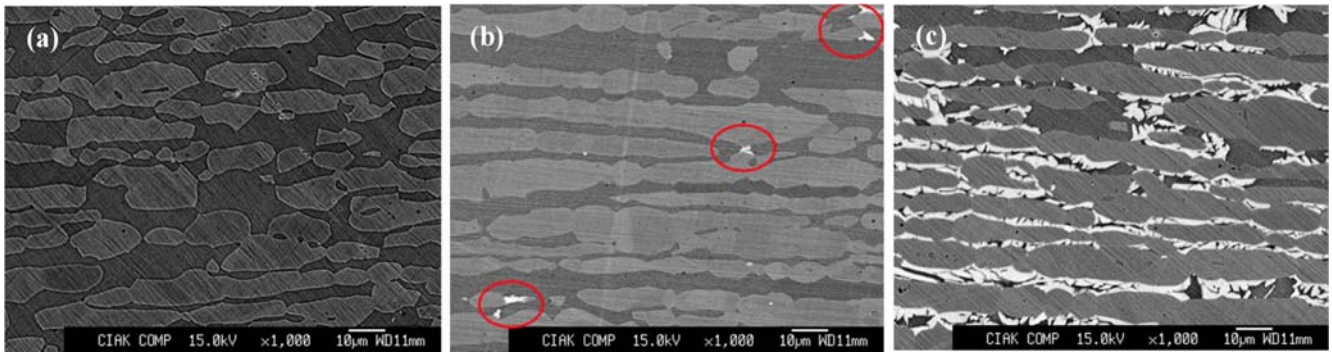

Fig. 10. BSE micrographs of SDSS annealed at 1100 ºC followed by quenching by (a) 1 °C/s, (b) 0.5 °C/s, and (c) 0.1 °C/s.

CCT diagram was in good agreement with the experimental observations.

ACKNOWLEDGMENTS

This work was supported by the National Research Foundation grant funded by the Korea government (MEST) through GCRC-SOP (Grant No. 2011-0030666) and from the Fundamental R&D Program for Core Technology of Materials funded by the Ministry of Knowledge Economy, Republic of Korea.

REFERENCES

1. J. Michalska and M. Sozanska, *Mater. Charc*. **56**, 355 (2006).
2. M. Martins and L. C. Casteletti, *Mater. Charc*. **55**, 225 (2005).
3. Y. J. Kim, L. S. Chumbley, and B. Gleeson, *Metall. Mater. Trans*. *A* **35**, 3377 (2004).
4. Y. J. Kim, O. Ugurlu, C. Jiang, B. Gleeson, and L. S. Chumbley, *Metall. Mater. Trans. A* **38**, 203 (2007).
5. J. I. Bae, S. T. Kim, T. H. Lee, H. Y. Ha, S. J. Kim, and Y. H. Park, *Korean J. Met. Mater*. **49**, 99 (2011).
6. D. Qiu and W. Z. Zhang, *Acta Mater*. **55**, 6754 (2007).
7. A. J. Ramirex, J. C. Lippold, and S. D. Brandi, *Metall. Mater. Trans*. *A* **34**, 1575 (2003).
8. J. O. Nilsson, P. Kangas, T. Karlsson, and A. Wilson, *Metall. Mater. Trans. A* **31**, 35 (2000).
9. S. S. M. Tavares, J. M. Pardal, L. D. Lima, I. N. Bastos, A. M. Nascimento, and J. A. de Souza, *Mater. Char*. **58**, 610 (2007).
10. A. J. Sedriks, *Corrosion of Stainless Steels*, John Wiley & Sons, New York (1996).
11. A. Gregori and J. O. Nilsson, *Metall. Mater. Trans*. A **33**, 1009 (2002).
12. R. Badji, B. Mabrouk, B. Bacroix, C. Kahloun, B. Belkessa, and H. Maza, *Mater. Char*. **59**, 447 (2008).
13. P. Sathiya, S. Aravinda, R. Soundararajan, and A. Noorul Haq, *J. Mater. Sci*. **44**, 114 (2009).
14. Y. J. Kim, L. S. Chumbley, and B. J. Gleeson, *Mater. Eng. Perf*. **17**, 234 (2008).
15. J. O. Nilsson, T. Huhtala, P. Jonsson, L. Karlsson, and A. Wilson, *Metall. Mater. Trans*. *A* **27**, 2196 (1996).
16. T. H. Lee, S. J. Kim, and S. Takaki, *Metall. Mater. Trans. A* **37**, 3445 (2006).